

SOLIDIFICATION, MACROSTRUCTURE AND SHRINKAGE FORMATION OF DUCTILE AND COMPACTED IRONS

Roberto E. Boeri , Marcos G. López , Nicolás E. Tenaglia , and Juan M. Massone 
 INTEMA, CONICET-University of Mar del Plata, Mar del Plata, Argentina

Copyright © 2020 American Foundry Society
<https://doi.org/10.1007/s40962-020-00444-z>

Abstract

This manuscript summarizes recent investigation of the authors into the solidification and shrinkage defect formation of ductile and compacted graphite cast irons. The study makes use of the DAAS (direct austempering after solidification) technique, developed earlier by some of the authors, to reveal the solidification grains. In addition, color metallography is used to reveal the microsegregation pattern. The formation of shrinkage defects is related to both the solidification macrostructure and the microsegregation pattern. The examination of the macrostructure shows that large solidification grains, composed by dendritic austenite and graphite, characterize the solidification of compacted graphite irons of carbon equivalent values ranging from hypoeutectic to hypereutectic. Similar results are observed for ductile iron, but in this case, the hypereutectic irons display a finer macrostructure. The

characteristics of the primary austenite dendrites are revealed by the microsegregation pattern, which is exposed by the color etching reagent. This pattern also clarifies the nature of the interaction between the growing austenite and the compact and spheroidal graphite particles. The microshrinkage cavities in both ductile and compacted graphite irons form at the interior of the austenite grains, where fluid feeding cannot compensate the contraction of the last-to-freeze portions of the melt. Schematics of the solidification of ductile and compacted irons are proposed, accounting for the experimental observations.

Keywords: ductile iron, compacted graphite iron, solidification, shrinkage, carbon equivalent, DAAS

Introduction

Both ductile iron (DI) and compacted graphite cast iron (CGI) are very competitive cast materials that are used in many industrial applications. However, the increasing demand on the properties of the finished products, along with the pressure to reduce costs, creates a great need for consistently producing better-quality castings. A major problem affecting DI and CGI castings is the presence of microshrinkage defects that can affect the mechanical properties of the irons and often lead to the rejection of the parts. In particular, when high-strength pieces are produced, it is critical to ensure that they are structurally sound. Avoiding the presence of microshrinkage demands

a thorough understanding of its origin; nevertheless, in most of the published works, the study of the influence of different factors on porosity follows an empirical treatment. Extensive work is found in the literature regarding factors affecting shrinkage porosity in cast iron. Among others, the influence of the mold media and inoculant type,¹ phosphorous content,² dissolved gas in the liquid phase³ and rare earth content⁴ on the shrinkage characteristics has been studied. Microshrinkage forms during solidification, and its location is governed by the distribution of the last remaining liquid phase at the end of solidification. Therefore, the shape of the solid dictates the location and distribution of the microshrinkage cavities. Nevertheless, there is not a complete agreement on the features of the solidification of DI and particularly of CGI.

Since DI discovery, and more recently CGI, significant research efforts have been focused on the study of the nucleation and growth of graphite, accounting for its

This paper is an invited submission to IJMC selected from presentations at the 6th Keith Millis on Ductile Iron held October 23–26, 2018 at the Sonesta Resort, Hilton Head Island, SC. It is published in the IJMC by permission of the DIS (Ductile Iron Society).

different morphologies. Austenite nucleation and growth, on the other hand, received much less attention. Over the last two decades, investigations into the solidification macro- and microstructures of DI and CGI provided some key results.⁵⁻¹³ Two experimental techniques were particularly useful for these investigations. First, a color etching reagent that reveals the microsegregation pattern of Si allowed to identify the shape of primary austenite dendrites and the location of the last-to-freeze (LTF) portions of melt. In addition, another key technique called direct austempering after solidification (DAAS)^{5,6} was developed to reveal the ingot macrostructure of normally solidified SGI parts, showing the presence of austenite grains of different sizes. Later, the correspondence of the grains revealed by DAAS with volumes of the same crystalline orientation was verified by using electron backscattered diffraction on samples of SGI and lamellar graphite iron (LGI).^{14,15} DAAS was further employed by Elmquist et al.^{16,17} to study the relation between shrinkage porosity and the solidification structure of LGI.

The use of these techniques, individually or combined, provided interesting results, revealing the shape and extension of the austenite grains and the shape of the eutectic colonies or cells. In the case of DI, the results supported earlier sketches of the solidification proposed by Engler.¹⁸

The results described above gave experimental support to an explanation of the solidification of these types of free graphite cast irons.^{8,10,13} The proposed models, schematized in Figure 1, state that for both DI and LGI, the solidification starts with the independent nucleation and growth of austenite dendrites and graphite from the melt. As dendrites grow, they collide with each other, defining the grains that can be observed macroscopically. The interaction of austenite and graphite is largely affected by the graphite growth morphology. In the case of DI, coupled

growth is not possible. As austenite dendrite arms contact graphite spheroids, these become enveloped and further growth of graphite is controlled by C diffusion through the austenite envelope. In the case of LGI, the interaction between austenite dendrites and flake graphite leads to the formation of eutectic cells or colonies, which grow cooperatively with both phases in contact with the melt. In both DI and LGI mechanisms, each austenite grain contains many graphite particles. The structure and distribution of the austenite grains can be observed after DAAS. The shape and size of the eutectic cells or colonies, if they are present, can be determined by color etching.

The revision of the literature specific for DI and CGI suggests that the knowledge about the formation of microshrinkage could be improved by the characterization of the solidification macro- and microstructures by means of DAAS and color etching, which should allow for better understanding of the relationship between primary austenite morphology and defect formation. Therefore, this investigation will focus on the characterization of the macrostructure of DI and CGI and its correlation with the formation of shrinkage defects.

Design of Experiments

Melts

All tests were carried out on samples obtained from cast iron heats made at the foundry laboratory of INTEMA. Three experimental melts were prepared by using a medium-frequency induction furnace of 50 kg capacity. Pig iron, steel scrap, ferroalloys and carbon raiser were used as raw materials. A standard melting procedure was used for all heats. After meltdown, the chemical composition was adjusted, and the temperature was raised to 1500 °C, where the liquid metal was held for 10 min. Then, the melt was

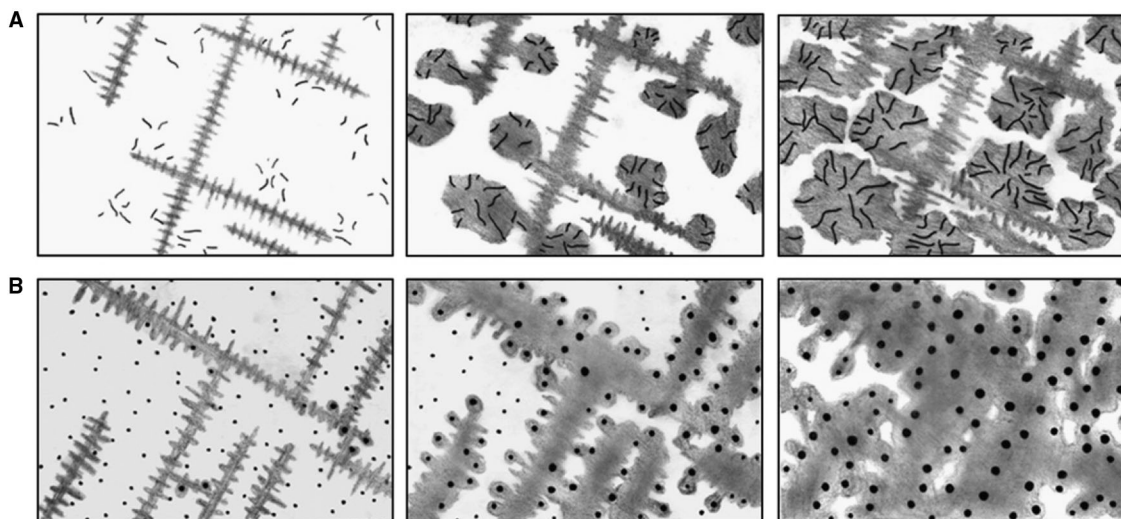


Figure 1. Schematic proposal of LGI (a) and DI (b) solidification.¹²

tapped into a 30-kg treatment ladle. For Melts A and B, where compacted graphite morphology was aimed, 0.6% FeSiMg(6%Mg) alloy was added through a sandwich-type treatment, while post-inoculation was performed with 0.5% of FeSi(75%Si). In the case of melt C, where spheroidal graphite was aimed, the melt was treated with 1.6% of FeSiMg(9%Mg) and inoculated with 0.65% FeSi(75%Si). Pouring temperature was 1400 °C. Compositions included small amounts of Cu and Ni that were added to reach the level of austemperability needed to carry out the DAAS procedure.⁶ The chemical compositions of the heats are listed in Table 1. Melts A and C are approximately eutectic, while melt B is hypereutectic.

Molds

Molds were prepared using resin-bonded silica sand. The casting used in this work was designed with the objective of producing shapes with shrinkage defects which can be heat-treated according to the DAAS procedure to be able to reveal the macrostructure. The design, as shown in Figure 2, intentionally includes dimensions and geometric relations that violate the rules of sound castings. The pattern includes three shapes of interest. SC and SB are cylinders of 20 and 35 mm of diameter. SA is a 25-mm-diameter cylinder with hemispherical top, located on top of a cube. The ability of the casting to produce microshrinkage was verified by the solidification software MagmaSoft.

The solidification time for each shape was also calculated by this software. Calculated values were 160, 360 and 275 s for SC, SB and SA, respectively. The simulation was also used to assess the proper shake-out time to proceed austempering. The shake-out time is defined as the time elapsed from the completion of the mold filling to the instant when the part is taken out from the mold. At shake-out, the part must be solid, but the temperature of the relevant volumes needs to be above the critical temperature range for the beginning of the decomposition of austenite.

Figure 3 shows the predicted profile of porosity at the middle section of the casting for a eutectic DI. As intended, different portions of the casting show shrinkage defects.

DAAS

The DAAS technique was applied to reveal the macrostructure of the CGI and DI samples.⁶ The thermal cycle used is plotted in Figure 4. After pouring and solidification completion (Point 2), the casting was shaken out when the minimum temperature of all shapes of interest was above approximately 950 °C (Point 3). Then, the casting was rapidly transferred to a furnace held at 920 °C, where it was kept for 30 min to allow for temperature homogenization (Point 4). The following step involved the austempering in a molten salt bath held at 360 °C for

Table 1. Chemical Composition in wt%

Melt ID	%C	%Si	%Mn	%S	%P	%Mg	%Cu	%Ni
A	3.38	2.74	0.17	0.017	0.033	0.020	0.97	0.66
B	3.53	3.15	0.18	0.016	0.041	0.015	1.02	0.78
C	3.31	2.76	0.13	0.021	0.039	0.053	0.85	0.53

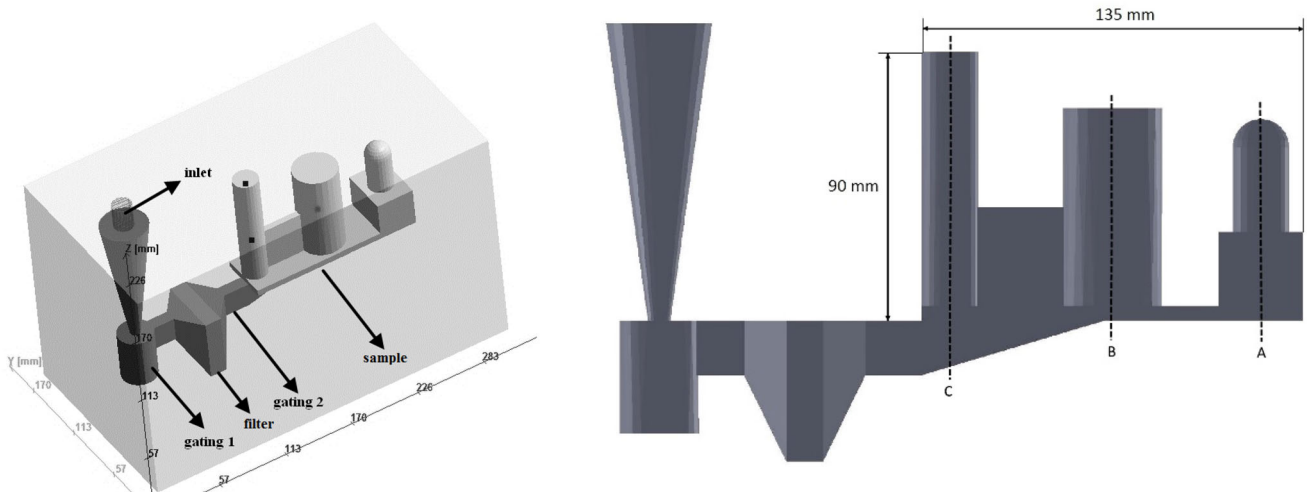


Figure 2. Sketches of the experimental casting. Dimensions in millimeters.

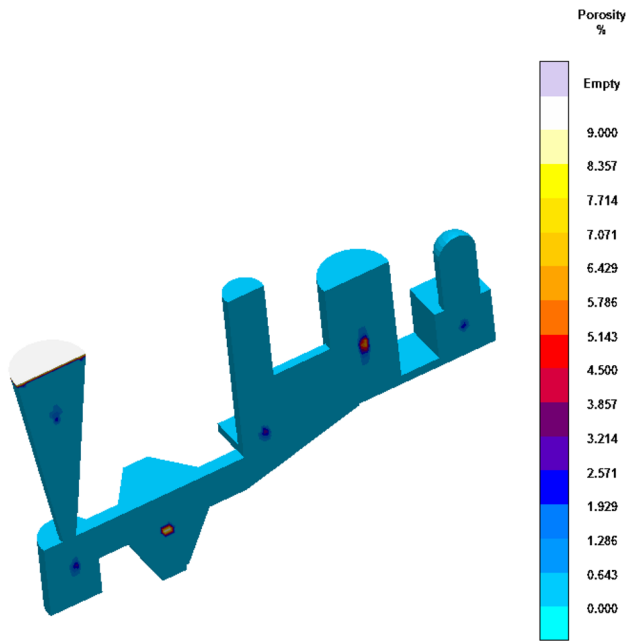


Figure 3. Simulation of solidification showing shrinkage formation.

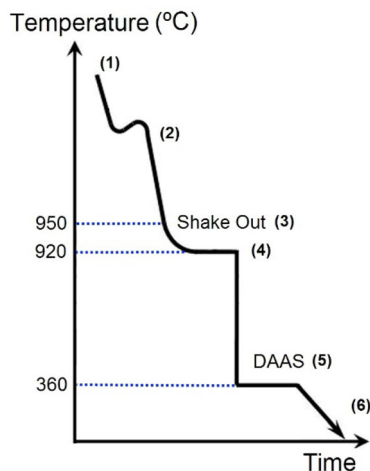


Figure 4. Thermal cycle of DAAS technique.

90 min (Point 5). Finally, the casting was cooled down to room temperature (Point 6).

Metallography and Color Etching

After performing the DAAS technique, the shapes of interest were cut from the casting and sectioned along different planes. The macrostructure of the DAAS-treated samples was revealed after polishing and etching with 2% Nital. Etching time or nitric acid concentration in the reagent can be adjusted to obtain the best contrast. The graphite microstructure was characterized by comparison with standard charts (ASTM A247). The solidification microstructure of the samples was revealed by color

etching technique using Motz reagent, a solution that is comprised by 10 g NaOH, 40 g KOH, 10 g picric acid and 50 ml of distilled water. Etching was carried out for 60 s at the boiling temperature of the solution. In all cases, samples were ferritized before color etching. This practice is recommended to obtain the best correspondence between color mapping and Si concentration.

Results

Micro- and Macrostructure of CGI

Figure 5 shows the graphite morphology obtained for CGI Melts A and B. Graphite particles are mainly vermicular. The average of five fields per sample showed that Melt A has a nodularity of 30%, whereas Melt B has a nodularity of 15%. These values are consistent with the amounts of Mg found in each melt.

The microstructure after Nital 2% etching is shown in Figure 6. As a result of the austempering heat treatment involved in the DAAS technique, the matrix microstructure is formed by a fine mixture of acicular ferrite and retained austenite, usually called ausferrite. Thanks to the relatively high austempering temperature employed, the amount of retained austenite found at room temperature is high. This austenite is a fraction of the primary solidification austenite.

After standard chemical etching with Nital (2%), the grained structure of the austenite is revealed macroscopically, as shown in Figures 7 and 8. Small equiaxed grains are present at the faster solidifying portions of the sample, while larger, and in some cases columnar, grains are observed on other areas.

Shrinkage defects are difficult to identify in Figures 7 and 8. A higher magnification observation, as shown in Figure 9, shows the location of the microshrinkage defects inside a large austenite grain placed at the thermal center of the sample shown in Figure 7a. The defects observed in Figure 9 display some orange coloring that is caused by the oxidation of the shrinkage cavities. A dotted line has been used to mark the grain boundary. The shrinkage is inside the grain and not along the grain boundary. A higher magnification metallography of the microshrinkage is shown in Figure 10. Shrinkage appears as disperse irregular cavities, clearly distributed following an intradendritic pattern. As the sample is inspected at the surroundings of the area showing noticeable shrinkage of Figure 9, still some smaller isolated shrinkage can be found, as shown in Figure 11.

After color etching of Melts A and B, the dendritic pattern of the austenite, not visible under regular Nital etching, can be recognized. Figure 12 shows a low-magnification

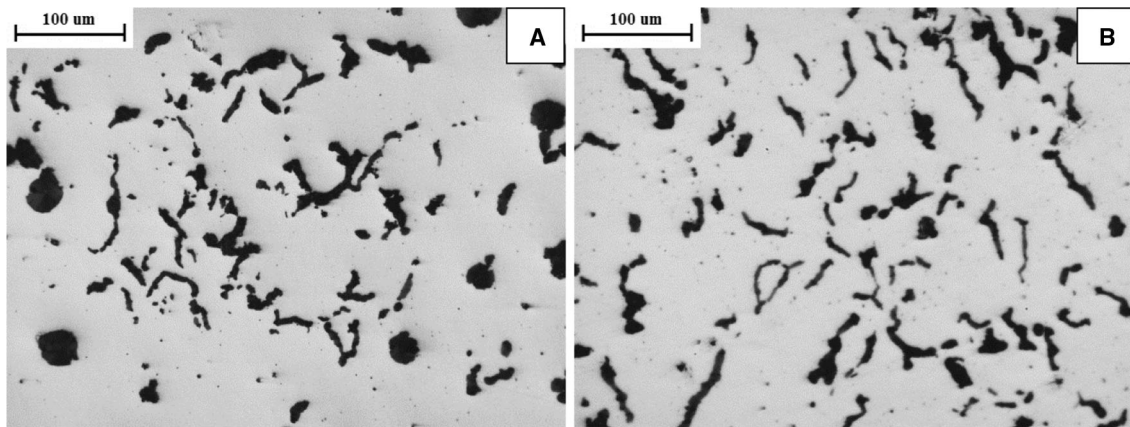


Figure 5. Microstructure of Melt A (left) and Melt B (right). Unetched.

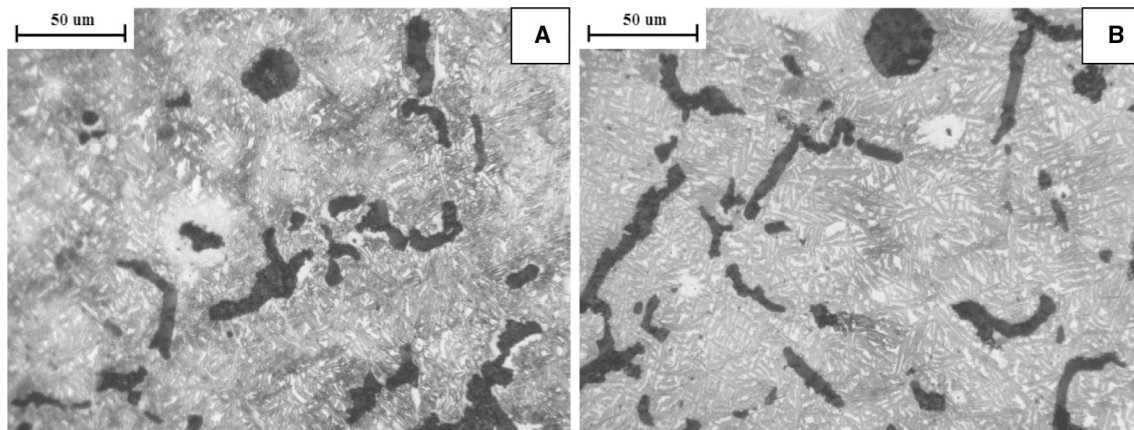


Figure 6. Microstructure of Melt A (left) and Melt B (right) after etching with Nital 2%.

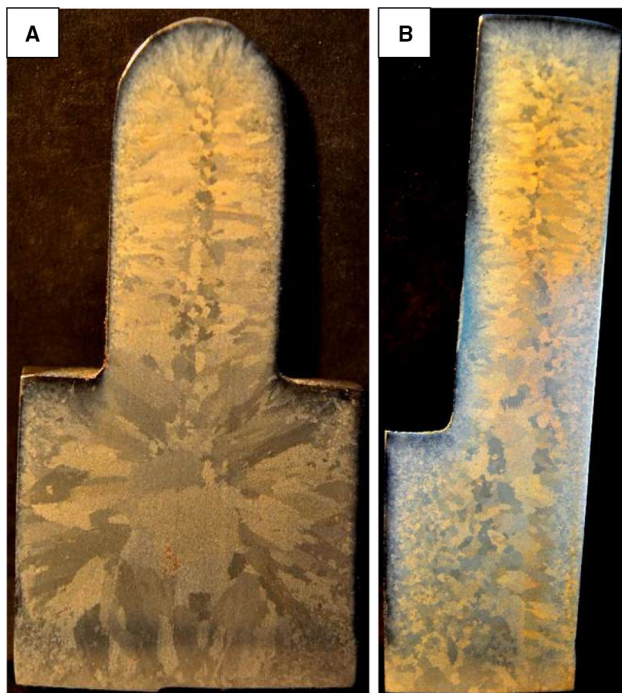


Figure 7. Solidification macrostructures of Melt A, shape SA (a) and SC (a).

metallography covering a large area (note the scale bar). Microsegregated LTF portions are colored in brighter yellow. The area shown in Figure 12 is inside one macroscopic grain from the columnar zone of Melt B. Note that some nearly round patterns surrounded by microsegregation can be recognized, particularly at the right-hand side of the metallography. These round areas correspond to “eutectic cells.”

As color-etched samples are observed at higher magnification, as shown in Figures 13 and 14, the intragranular or intradendritic nature of the microsegregation is evident. The location of the LTF liquid, the position where microshrinkage can form, is revealed by the brighter yellow color, corresponding to the areas having the lower local concentration of silicon. Note that although the brighter yellow portions may look like second-phase precipitates or carbides, they are not such phases. The microstructure is free from unwanted phases, as shown in Figures 5 and 6.

The observations of the micro- and macrostructures shown in this study and the results of previous investigations^{14,15,19} give support to explain the solidification of CGI in a similar manner of what has been proposed for



Figure 8. Solidification macrostructures of Melt B, shape SA (a) and SC (b).

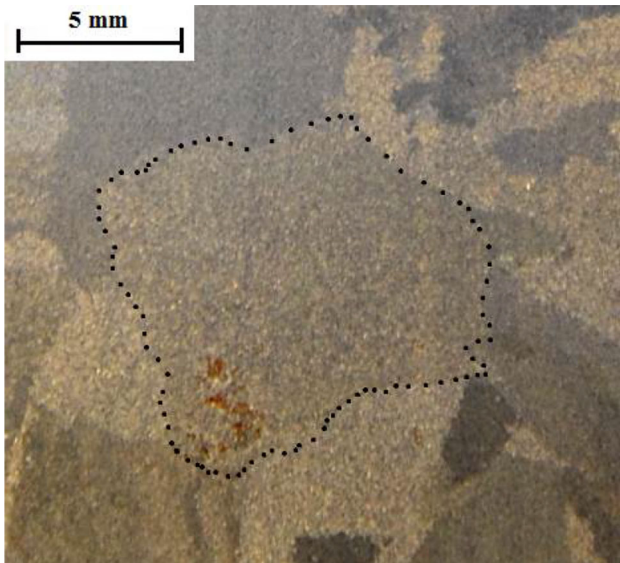


Figure 9. Grain at the thermal center of a sample of Melt A, showing the location of the microshrunk areas, revealed as rust.

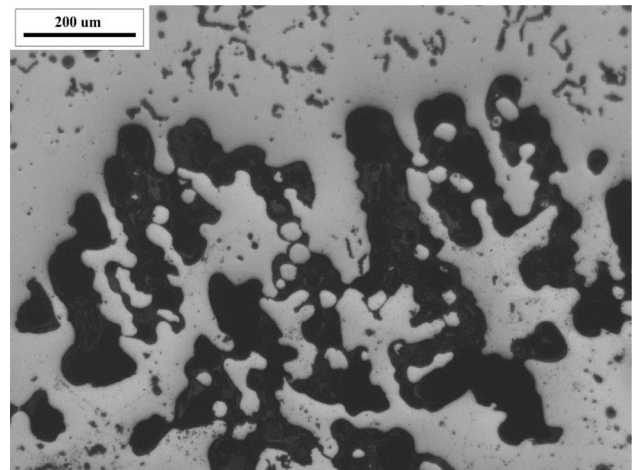


Figure 10. Optical microscopy of portions of the shrinkage shown in Figure 9.

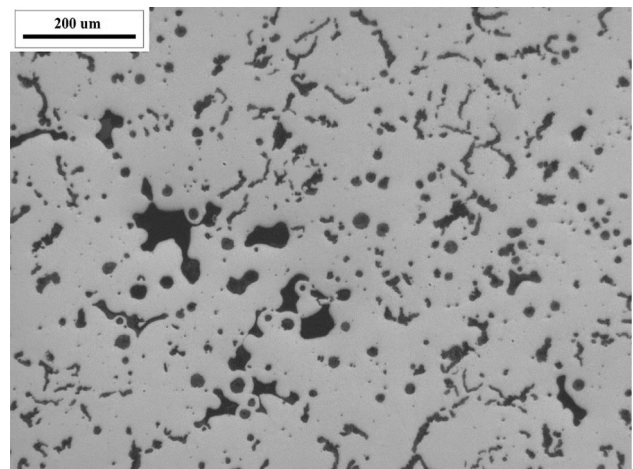


Figure 11. Smaller microshrinkage voids on Melt A.

LGI, as shown in Figure 1. The nucleation and growth of the austenite dendrites and graphite proceed independently in the melt. The graphite particles grow initially in the melt but later, as the growing austenite dendrites get in contact with them, form eutectic colonies in which austenite and graphite grow cooperatively, with both phases in contact with the melt, as it was formerly proposed by Mampaey¹⁹ in his analysis of partially solidified samples. The portions of the casting exposed to greater cooling rates reach larger undercoolings and show a relatively large density of austenite nuclei, resulting in small grain size. On the other hand, slower cooling portions show smaller density of austenite nuclei and therefore larger grain size. Each one of these grains contains many eutectic colonies in it. A transition between columnar and equiaxial grains is observed in both heats for the different geometries poured. Spheroidal graphite precipitates, present in different amounts along CGI castings, appear to be enveloped by austenite at early stages of solidification, as indicated by the color etch in Figures 13 and 14.

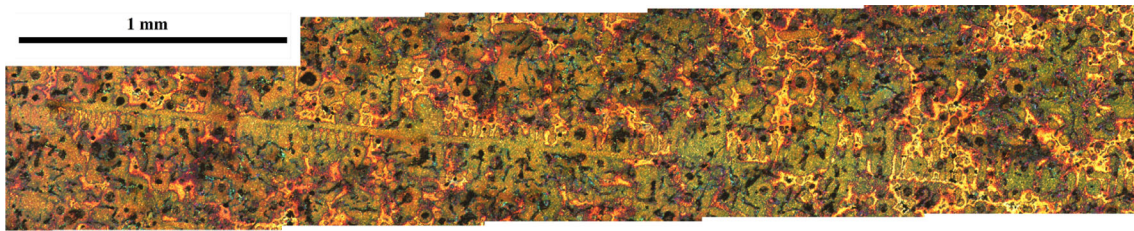


Figure 12. Microstructure of Melt B. Color-etched.

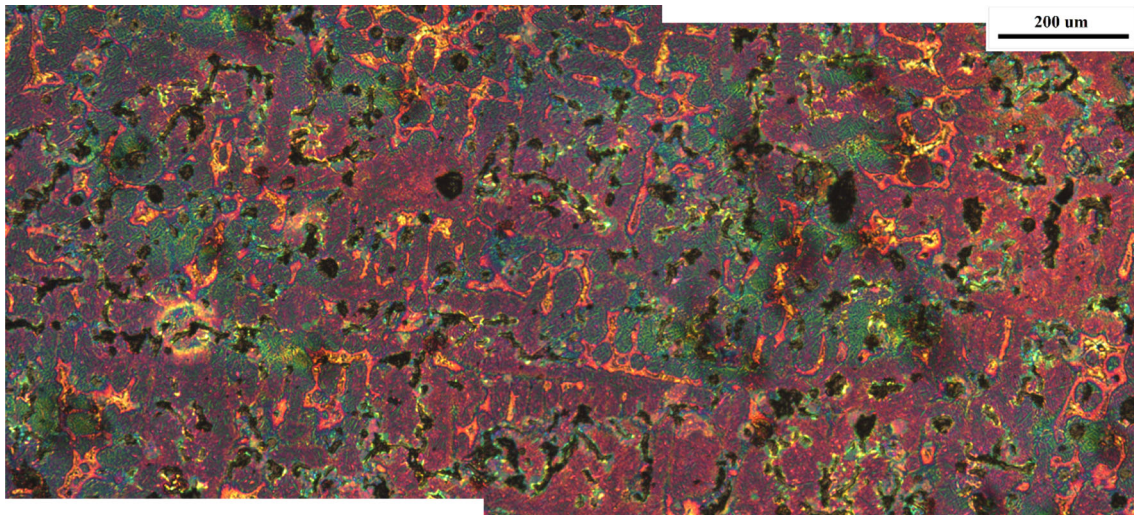


Figure 13. Microstructure of Melt A. Color-etched.

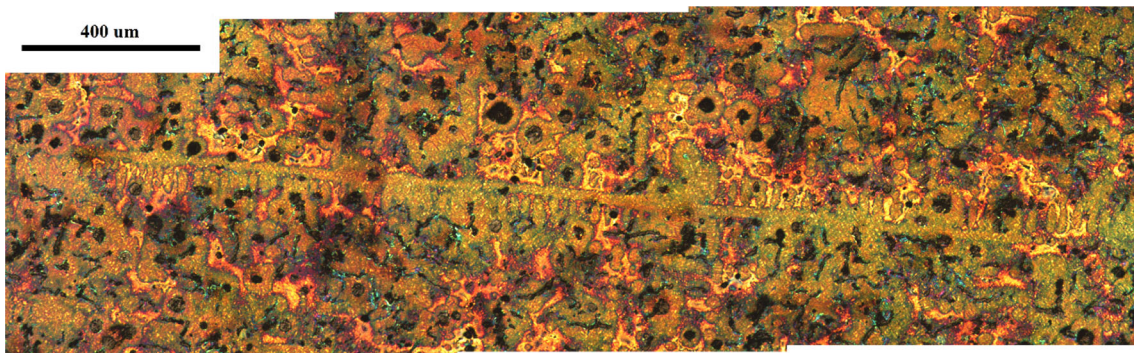


Figure 14. Microstructure of Melt B. Color-etched.

Explanation of the Solidification of Hypereutectic CGI

The solidification mechanism described above appears to be valid regardless of the carbon equivalent value, as for a hypereutectic melt, such as Melt B, relatively large primary austenite dendrites, from which the eutectic colonies or cells can grow, are also found (Figures 8:14). This finding may be unanticipated as the primary proeutectic phase is graphite, and the formation of austenite dendrites is not initially expected. Some authors sustain that under this condition, austenite should grow coupled with compacted graphite, taking the shape of nearly spherical cells.^{20,21}

Nevertheless, Fredriksson^{22,23} showed that the coupled zone of the Fe–C eutectic is asymmetrical, as represented schematically in Figure 15. Accordingly, the solidification of hypereutectic melts of CGI and LGI can proceed as represented in Figure 15, where the red line represents the concentration of C in the liquid as a function of temperature. As hypereutectic liquid cools below L/Gr equilibrium temperature a certain ΔT_{Gr} , nucleation of graphite from the melt will start (Point 1). The shape of the graphite will be different depending on the treatment of the melt before pouring, and the density of nuclei per unit volume will be controlled by the inoculation practice. As cooling proceeds, hypereutectic graphite will continue to grow and eventually

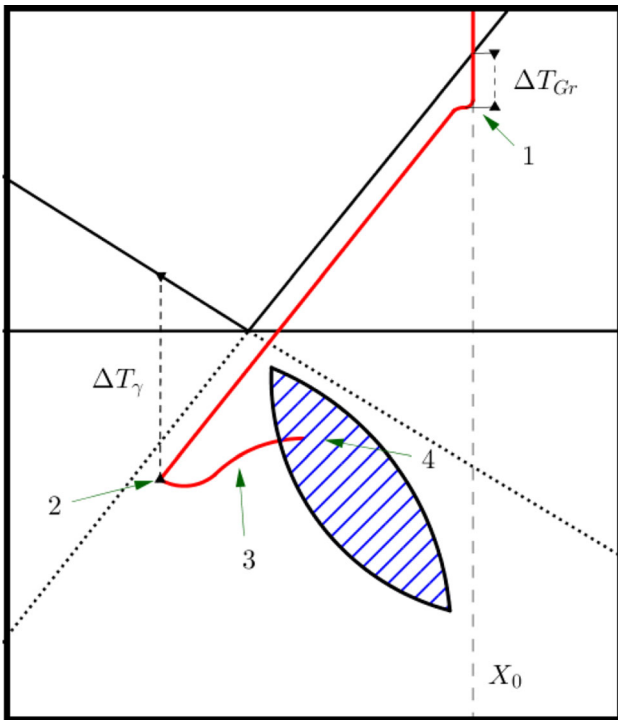


Figure 15. Plot of the C concentration of the melt as solidification of hypereutectic CGI proceeds.

continue nucleating, in contact with the melt. The remaining liquid will be progressively impoverished in C. At some temperature (Point 2), the melt will be

supercooled enough with respect to the γ -Gr equilibrium temperature to nucleate and grow austenite. Under this condition, austenite can grow rapidly into the melt, rejecting C and causing an increase in the C concentration of the melt. Coupled growth, as explained by Fredriksson, cannot proceed at Point 2. The temperature plot can show recalescence as the austenite releases latent heat (Zone 3). The concentration of C in the liquid increases progressively along Zone 3, until it reaches the coupled growth zone, where coupled growth can take place and eutectic cells will grow until all liquid is exhausted. Recent investigations, as described above, provided a clear proof of the morphology assumed by austenite during solidification. The experiments using DAAS show that at the low-cooling-rate portions of the castings of CGI, austenite grows dendritically, forming relatively large grains. The formation of eutectic cells in CGI arises from the interaction of austenite dendrite arms and the compacted graphite particles at the coupled zone of Figure 15. The cell growth takes place inside a large austenite grain originated earlier during the solidification. Consequently, the concept of an asymmetric coupled zone for CGI explains the existence of primary γ even for hypereutectic compositions of CGI where coupled growth can take place.²⁴⁻²⁶

The formation of dendrites of austenite is somehow easier to understand in the case of DI, as coupled growth is not possible, and a eutectic cell cannot be defined. This is because DI presents a divorced eutectic, in which the

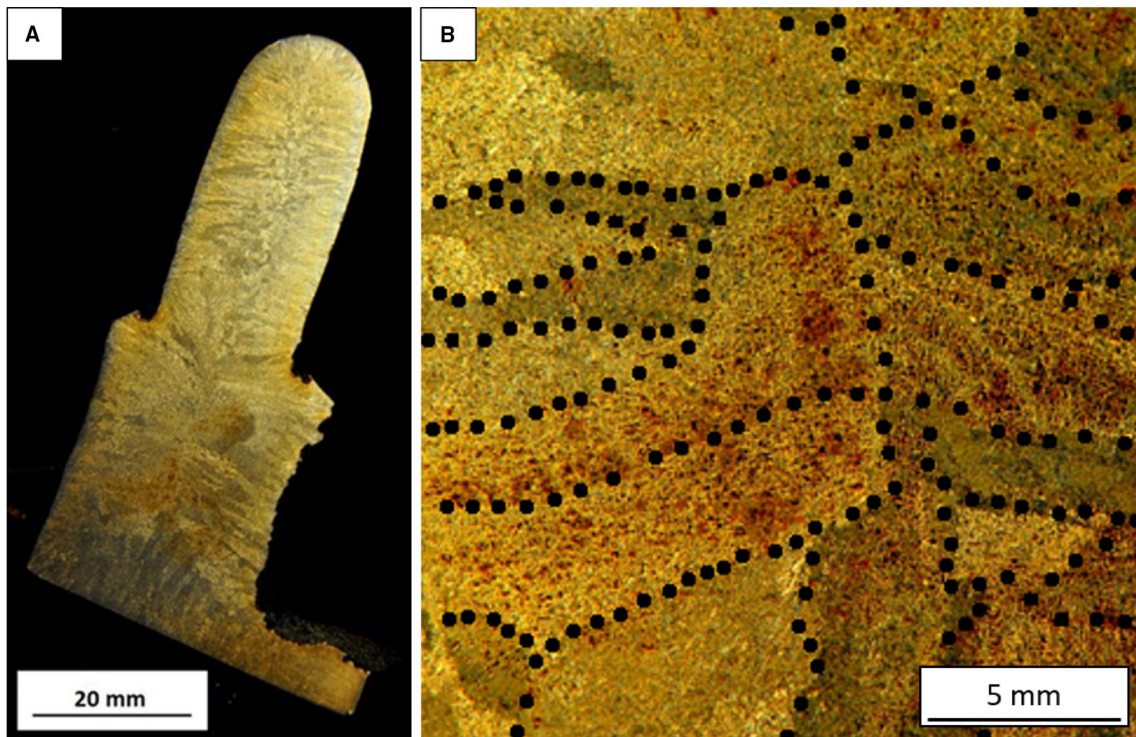


Figure 16. (a) Solidification macrostructure of sample SA of Melt C. (b) Distribution of shrinkage defects in the same sample.

spheroidal graphite nodules are quickly surrounded by an austenite shell after they nucleate in the liquid and have no further contact with the melt.²⁷ Thus, the only growth mechanism left for the austenite is dendritic. The size of the austenite grains in the case of hypereutectic DI is smaller than that for eutectic and hypoeutectic melt. The explanation of this characteristic is still unclear.

Shrinkage Defects on DI

DI Melt C showed 95% nodularity. As the macrostructure of DI as revealed by DAAS has been discussed earlier,⁵⁻⁸ this section will focus on the study of microshrinkage. The solidification macrostructure revealed at the cross-section of one sample of Melt C subjected to DAAS is shown in Figure 16a. A typical grained structure can be seen, characterized by the presence of equiaxed and columnar grains. As shown in Figure 9, the central part of the sample displays some orange coloring that is caused by oxidation induced by the presence of the dispersed shrinkage. Figure 16b shows the distribution of the shrinkage defects through the grains. The grain boundaries have been marked by dotted lines.

The area showing shrinkage cavities was examined by SEM. Figure 17 shows that the shrinkage cavities form between the arms of a dendrite, inside an austenite grain.

The result of color etching of a shrinkage-free portion of the sample of Melt C corresponding to Figure 16 is shown in Figure 18. The color mapping indicates that noticeable microsegregation takes place inside the austenite grains. In this case, LTF regions as those marked by arrows appear as isolated portions surrounded by red halos. Figure 19 shows color-etched regions where shrinkage is found. Relatively larger cavities of size in the order of hundreds of microns, as those shown in Figure 19a and b, do not appear to be located at LTF zones, as indicated by the color fringe surrounding them. Nevertheless, when apparently sound portions of the matrix are examined in detail, very small

shrinkage cavities, of size comparable to that of graphite particles, can be found at the LTF, as shown in Figure 19c, where a small cavity is located at an LTF.

Future Work and Potential Improvements

Refining the solidification structure is generally associated with improvements in the soundness and strength of castings as a result of finer distribution of microporosity, improved feeding, improved fluidity and greater homogeneity. The refining of the solidification structure has been a subject of great relevance for many non-ferrous alloys, as Al-Si alloys. Nevertheless, in the case of graphitic cast irons, the analysis has been usually limited to the characterization of the shape and dispersion of graphite. The primary austenite solidification structure, responsible for the morphology and distribution of microshrinkage defects, was rarely studied, perhaps because it was very difficult to reveal. Nowadays, with the availability of the DAAS technique, it becomes possible to study the variables governing the grain size in DI and CGI. Perhaps, austenite

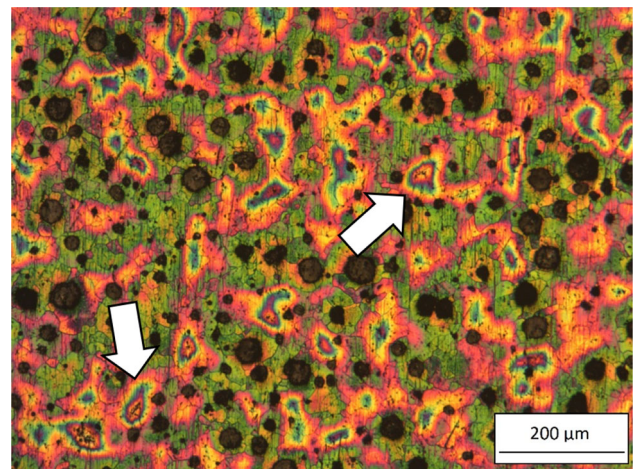


Figure 18. Microstructure of sample of Melt C at a shrinkage-free region.

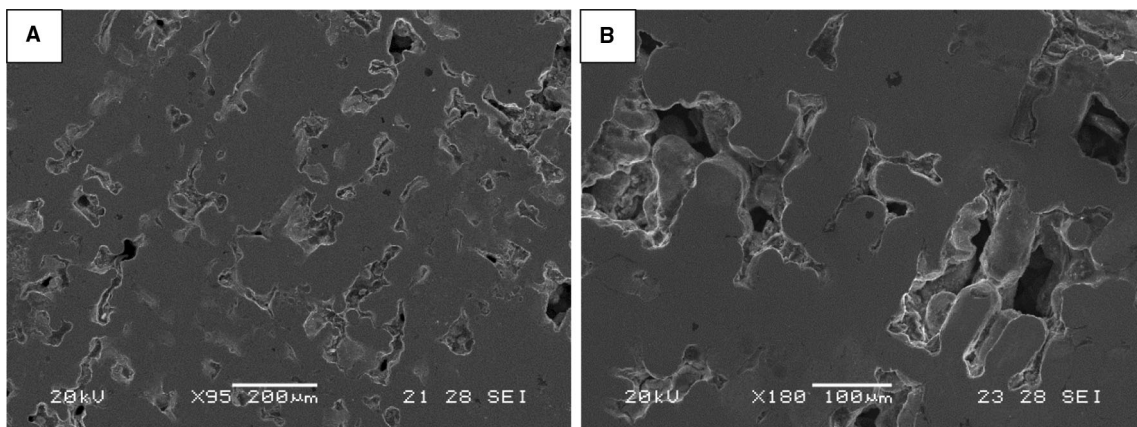


Figure 17. Shrinkage cavities from sample of Melt C examined by SEM.

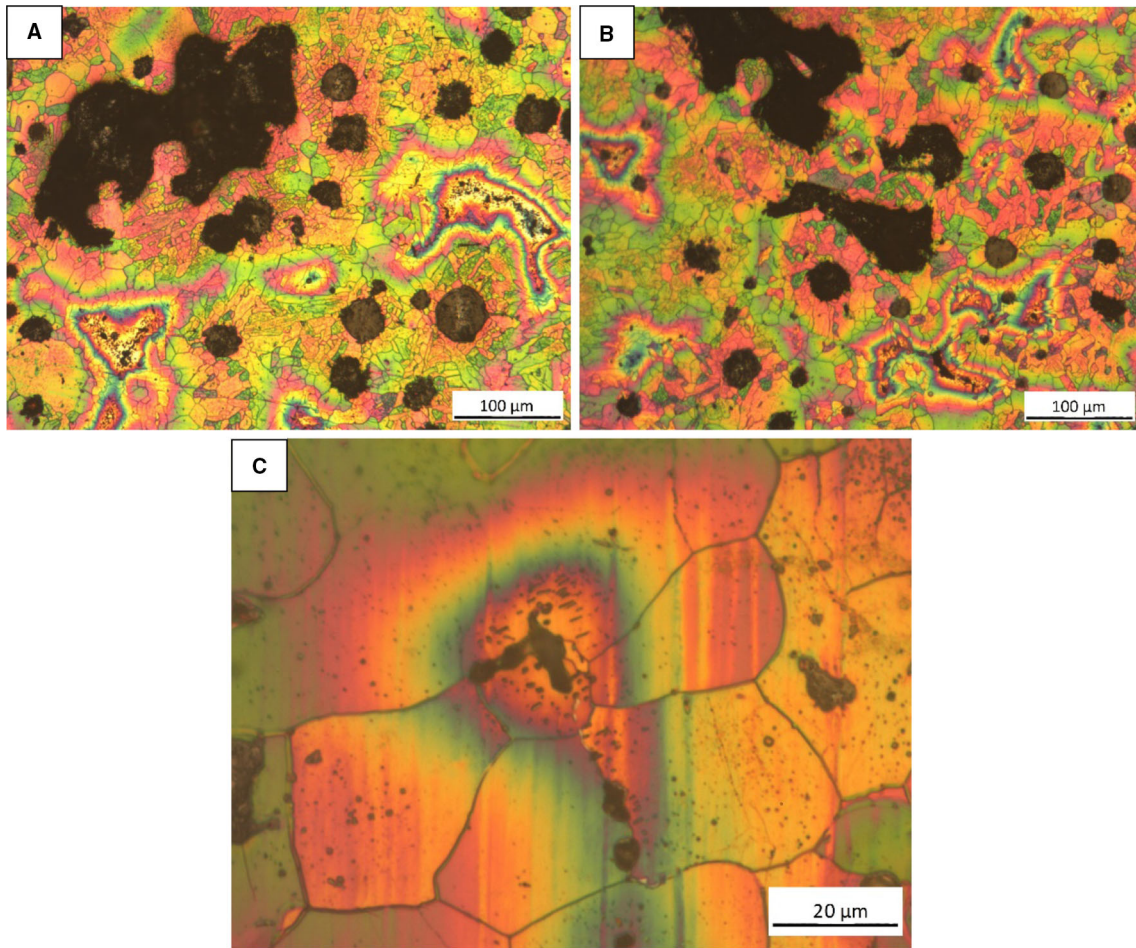


Figure 19. Microstructure of sample of Melt C at regions presenting shrinkage cavities. Color-etched.

nucleation can be improved by means of proper inoculation agents and the macrostructure refined in consequence, with potential benefits for the soundness of castings.

Concluding Remarks

Experimental results are consolidating the mechanism proposed to explain the solidification of DI and CGI. Some common features characterize the start of solidification, as in both cases austenite and graphite are proposed to nucleate independently from the melt. Nevertheless, as solidification proceeds, the interaction between austenite dendrites and graphite differs. CGI establishes coupled growth between austenite and graphite, generating eutectic cells. DI, on the other hand, cannot grow cooperatively. In both cases, a large amount of intradendritic liquid remains after dendrite coherency (grain size formation) has taken place.

The combined observation of macrostructure, microshrinkage and microsegregation has clarified the mechanism of formation of microshrinkage cavities.

Dispersed microshrinkage forms late during solidification, when a dendritic pattern of austenite is fully developed. As a result, shrinkage can only grow along the space between dendrite arms, getting its characteristic irregular shape. If the lack of liquid feeding takes place even later, smaller microshrinkage cavities form. In this latter case, the surroundings of the cavities are highly microsegregated, proving that they have formed at the LTF.

Acknowledgements

The study made use of an academic license of MagmaSoft, which is gratefully acknowledged.

Funding

This work was supported by MINCyT (PICT3038) and CONICET (PIP0558).

Conflicts of interest Not applicable.

Availability of data and material Not applicable.

Code availability Not applicable.

REFERENCES

1. M. Chisamera, I. Riposan, S. Stan, P. Toboc, T. Skaland, D. White, Shrinkage evaluation in ductile iron as influenced by mould media and inoculant type. *Int. J. Cast Metals Res.* **24**, 28–36 (2011)
2. T.S. Srivatsan, T.S. Sudarshan, The influence of phosphorus on shrinkage porosity in cast irons. *Mater. Lett.* **41**, 186–191 (1999)
3. G. Lesoult, Microporosity in cast alloys: simple consideration on its formation. *Int. J. Cast Metals Res.* **22**, 2–7 (2009)
4. K. Pedersen, N. Tiedje, Influence of rare earths on shrinkage porosity in thin walled ductile cast iron. *Int. J. Cast Metals Res.* **22**, 302–305 (2009)
5. G. Rivera, R. Boeri, J. Sikora, Revealing the solidification structure of nodular iron. *Cast Metals* **8**, 1–5 (1995)
6. G. Rivera, R. Boeri, J. Sikora, Revealing and characterising solidification structure of ductile cast iron. *Mater. Sci. Technol.* **18**, 691–697 (2002)
7. R. Boeri, J. Sikora, Solidification macrostructure of spheroidal graphite cast iron. *Int. J. Cast Metals Res.* **13**, 307–313 (2001)
8. G. Rivera, R. Boeri, J. Sikora, Research Advances in Ductile Iron Solidification. *AFS Trans.* **111**, 1–11 (2003)
9. G. Rivera, R. Boeri, J. Sikora, Influence of the inoculation process, the chemical composition and the cooling rate on the solidification macro and microstructures of ductile iron. *Int. J. Cast Metals Res.* **16**, 23–28 (2003)
10. G. Rivera, R. Boeri, J. Sikora, Solidification of gray cast iron. *Scripta Materialia* **50**, 331–335 (2004)
11. G. Rivera, R. Boeri, and J. Sikora, Searching for a unified explanation of the solidification of cast irons, *Eighth International Symposium Science and Processing of Cast Iron*, Beijing, China (2006), vol 1, pp. 45–50.
12. N. Tenaglia, R. Boeri, G. Rivera, J. Massone, Study of shrinkage porosity in spheroidal graphite cast iron. *Int. J. Cast Metals Res.* **29**, 112–120 (2016)
13. M. López, G. Rivera, J. Massone, R. Boeri, Study of the solidification structure of compacted graphite cast iron. *Int. J. Cast Metals Res.* **29**, 266–271 (2016)
14. G. Rivera, P. Calvillo, R. Boeri, Y. Houbaert, J. Sikora, Examination of the solidification macrostructure of spheroidal and flake graphite cast irons using DAAS and EBSD. *Mater. Charact.* **59**, 1342–1348 (2008)
15. L. Elmquist, K. Soivio, A. Diószegi, Cast iron solidification structure and how it is related to defect formation. *Mater. Sci. Forum* **790–791**, 441–446 (2014)
16. L. Elmquist, A. Diószegi, Shrinkage porosity and its relation to solidification structure of grey cast iron parts. *Int. J. Cast Metals Res.* **23**, 44–50 (2010)
17. L. Elmquist, A. Diószegi, T. Björklind, On the Formation of Shrinkage Porosity in Gray Iron Castings. *Key Eng. Mater.* **457**, 416–421 (2011)
18. A. Rickert, S. Engler, “Solidification morphology of cast irons”, *The Physical Metallurgy of Cast Iron*, *Mater. Res. Soc. Proc.*, 1985, pp. 165–174.
19. F. Mampaey, Influence of compacted graphite on solidification morphology of cast iron. *AFS Trans.* **27**, 11–17 (2000)
20. E. Frás, M. Górný, Inoculation effects of cast iron. *Arch. Foundry Eng.* **12**, 39–46 (2012)
21. N. Arab, Competitive nucleation in grey cast iron. *Arch. Foundry Eng.* **17**, 185–189 (2017)
22. H. Fredriksson, U. Akerlind, *Solidification and Crystallization Processing in Metals and Alloys*, 1st edn. (Wiley, London, 2012)
23. H. Fredriksson, The coupled zone in grey cast iron. *Metall. Trans.* **6A**, 1658–1660 (1975)
24. K. Pedersen, N. Tiedje, Solidification of hypereutectic thin wall ductile cast iron. *Mater. Sci. Forum* **508**, 63–68 (2006)
25. K. Olen, R. Heine, A revision of the Fe-C-Si system. *Cast Metals Res. J.* **4**, 28–43 (1968)
26. R. Heine, C. Loper, On dendrites and eutectic cells in gray iron. *AFS Trans.* **77**, 185–191 (1969)
27. D. Stefanescu, *Science and Engineering of Casting Solidification*, Springer, 2009.

Publisher’s Note Springer Nature remains neutral with regard to jurisdictional claims in published maps and institutional affiliations.